Published in "Astrophysical Jets", eds. D. Burgarella, M. Livio and C. P. O'Dea, 1993

THE M87 JET

J. A. Biretta

Space Telescope Science Institute
3700 San Martin Drive, Baltimore, MD 21218, USA

Abstract. We review the current observational status of the M87 jet at radio, optical, and X-ray frequencies. Special attention is paid to the radio morphology, the radio-to-X-ray spectrum, measurement of proper motions, and optical evidence for a counter-jet. The problem of jet confinement is discussed, as well as models for the radio-to-X-ray spectrum and the related problem of particle lifetimes. Finally a kinematic model is sketched wherein the first kpc of the jet is relativistic, followed by shocks and subrelativistic flow.

Table of Contents

1. INTRODUCTION

Seventy-five years ago H. D. Curtis noted a "curious straight ray" in M87 which was "apparently connected with the nucleus by a thin line of matter" (Curtis 1918). This observation marked the first discovery of an extragalactic jet, though its physical nature, as well as that of its host nebula, would remain obscure for several more decades. Later, Virgo A would be one of the first discrete sources discovered by the new "radio" astronomy, and its association with M87 (Bolton, Stanley, and Slee 1949) and the "curious" feature (Baade and Minkowski 1954) were quickly recognized. Eventually radio interferometer images revealed the bright radio lobes and the optical jet itself (Turland 1975). Similarly, the jet would be detected at X-ray frequencies, once the resolution was adequate to separate it from the bright thermal emission (Schreier, Gorenstein, and Feigelson 1982; Figure 1). While several hundred jets have now been discovered (Bridle and Perley 1984; Keel 1988; Fraix-Burnet et al. 1990; Liu and Xie 1992), M87 remains one of the nearest examples, making it an ideal target for study of the extragalactic jet phenomenon. Only one other extragalactic jet is substantially closer, and that is Centaurus A (NGC5128) which is at a very low declination and therefore is difficult to study with northern radio interferometers.

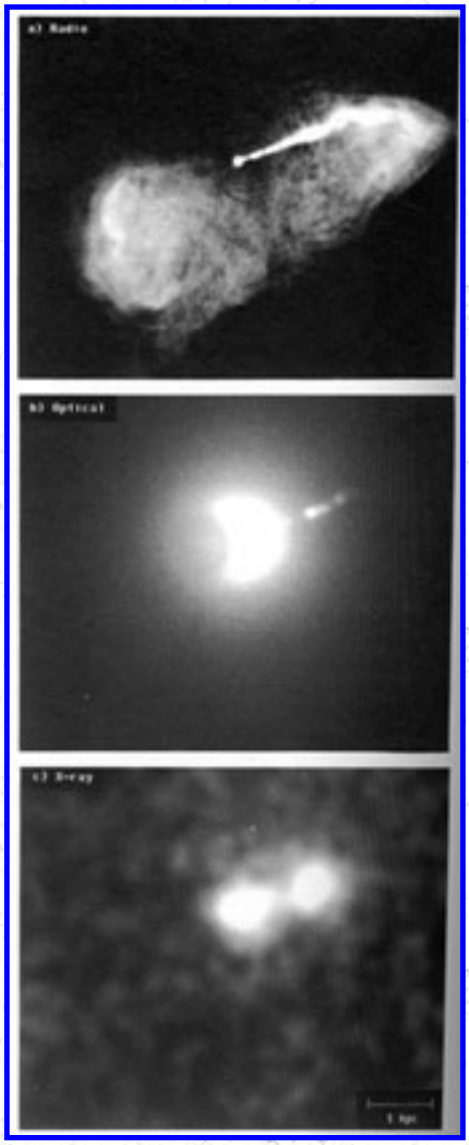

Figure 1. M87 at radio, optical, and X-ray bands. All images shown at similar scale, where 1 kpc = 12.8" assuming a distance of 16 Mpc. North is up. (a.) Radio image (5 x 10^9 Hz) at 0.4" resolution from VLA. Nucleus, jet, and radio lobes are prominent. (b.) Optical image (4 x 10^{14} Hz) obtained with Palomar 1.5 m telescope. Resolution 1.2". The nucleus, knots A, B, and C in the jet, and stellar light are prominent. (c.) X-ray image (2 x 10^{17} Hz) obtained with Einstein satellite. Resolution is ~ 3". Nucleus and knot A are evident. Original data from BSH91.

M87 (NGC4486) is now recognized as a giant elliptical (E0/1) galaxy near the center of the Virgo

Cluster. It is one of two dominant galaxies in the cluster, the other being NGC4472. The associated radio source (Virgo A, 3C274, 1228+127) is classified as an FR-I source based on its low luminosity (P_{178MHz} ~ 1 x 10^{25} W H^{-1}) and edge-darkened morphology (Fanaroff and Riley 1974). In spite of this classification, its one-sided jet is more typical of FR-II sources, and perhaps this is related to its situation near the FR-I/II division at P_{178MHz} ~ 3 x 10^{25} W H^{-1}. Bridle (1984) has also noted that it has an unusually weak core for a one-sided jet. Its distance has been measured to be 15.9 Mpc using a redshift independent technique (Tonry 1991; z = 0.0043). We will assume a distance of 16 Mpc throughout this paper; this gives a linear scale of 78 pc per arcsecond, and a proper motion of 1 milliarcsecond (mas) per year corresponds to 0.254*c*, where *c* is the velocity of light.

In the following section I review the present state of the observational material, and briefly describe some straightforward conclusions drawn from the observations. In Section 3 some problems posed by the observations, and a possible model for the kinematics, are discussed.

2. OBSERVATIONS AND SOME IMPLICATIONS

I will begin by describing the results of radio observations, where information is available over a very large range of spatial scales, and also review some simple interpretations drawn from these results. Next, the optical and X-ray observations will be considered and compared to the radio. Finally, new evidence for motion in the jet, and optical evidence for a counter-jet, are presented.

A. Radio Structure of the Jet

We now examine the morphology seen in total and polarized intensity radio images. We will begin on scales ~ 0.1 pc, working outward to scales ~ 50 kpc. One of the highest resolution images yet obtained of M87 is that of Spencer and Junor (1986; *c.f.* Baath et al. 1992). This 22 GHz VLBI image, with a resolution of 0.0015" (Figure 2), shows the bright radio core and a weak "jet-like" extension in the west. Perhaps the most important implication of this image is that it sets an upper limit to the size of the region responsible for collimating the jet. If we take the eastern bright point source to be approximately coincident with the central engine, then the initial jet collimation must occur on scales less than or around 1000 A.U.

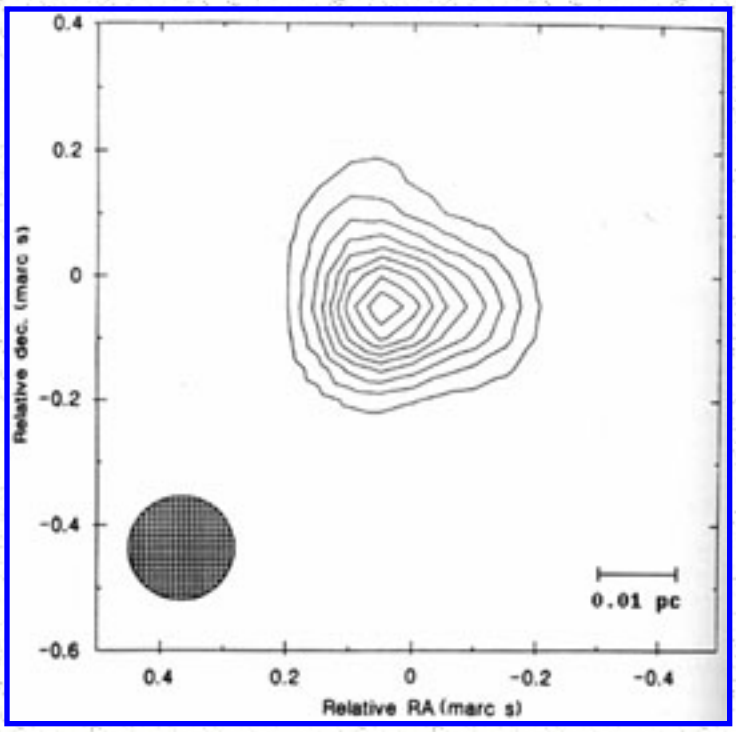

Figure 2. M87 nucleus observed with 22 GHz VLBI at 0.15 mas resolution (shaded circle). Peak brightness is 0.34 Jy beam^{-1} and the lowest contour is at 0.034 beam^{-1}. North is up. From Spencer and Junor (1986).

Moving to slightly larger scales, the 18 cm VLBI image of Reid et al. (1989) shows a well collimated jet about 20 pc long emanating from the nucleus (Figure 3). The opening angle of the jet on this scale is 10 degrees (full-width-quarter-maximum), which is only slightly broader than that seen at 1 kpc, indicating that most of the jet collimation has already occurred at this scale ~ 20 pc. The jet also appears to be limb-brightened at several points, due in part to a "filamentary" structure which appears to oscillate from one side of the jet to the other. For example, around 54 mas from the core the jet is brightest at the northern limb; the ridgeline then moves to the southern limb around 60 mas from the core, and then back to the northern limb by about 70 mas from the core.

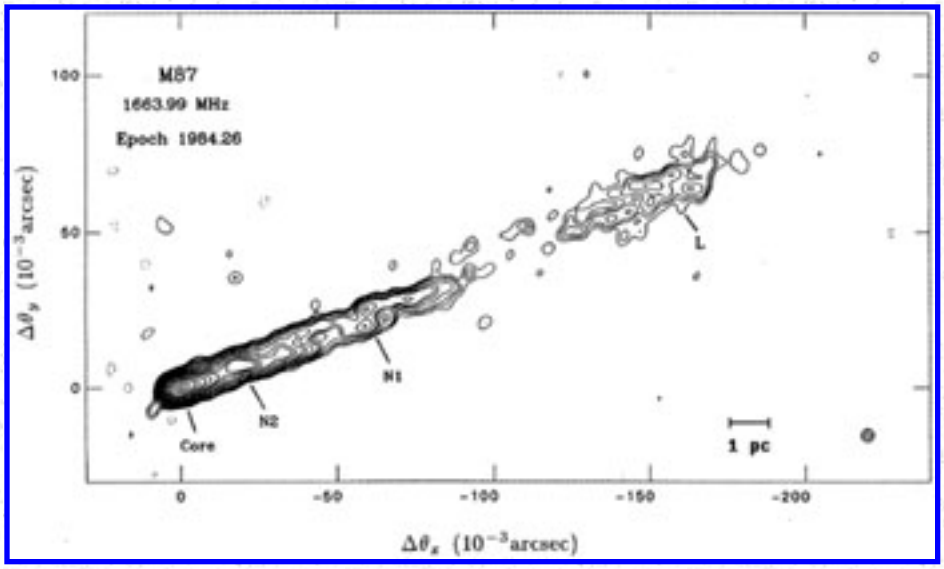

Figure 3. M87 nucleus at 1.66 GHz observed with World Array VLBI. Knots L, N1, and N2 are labeled. The resolution is 4 mas (shaded circle). The brightest region at the nucleus contains 0.97 Jy beam^{-1} while the lowest contour is at 2 mJy beam^{-1}. North is up. From Reid et al. 1989.

Similar morphologies are seen on scales to about 1 kpc (12 arcseconds). Figure 4 shows a 15 GHz VLA image of the M87 jet at 0.1" resolution (Owen, Hardee, and Cornwell 1989, hereinafter OHC89). What I will call the "inner jet" - that is, the region from the nucleus to knot A - roughly defines a cone with straight sides and an opening angle of 6 degrees (FWQM). There are many places along the inner jet where the structure is brighter at either or both limbs than in the jet center (*i.e.* limb-brightened). For example, in knot E, between knots E and F, and again between F and I, the edges of the jet are brighter than the jet center. There are also regions where one limb is particularly bright, such as in knots D and E. Filamentary or long, linear features are also evident in this region. For example, it is possible to follow the brightness ridgeline through knot D along a line which starts at the northern limb near the nucleus, crosses to the southern limb and back near the middle of the knot, and then slowly curves back towards the jet center as we move away from the nucleus. Pieces of similar features are also apparent in knots E and F.

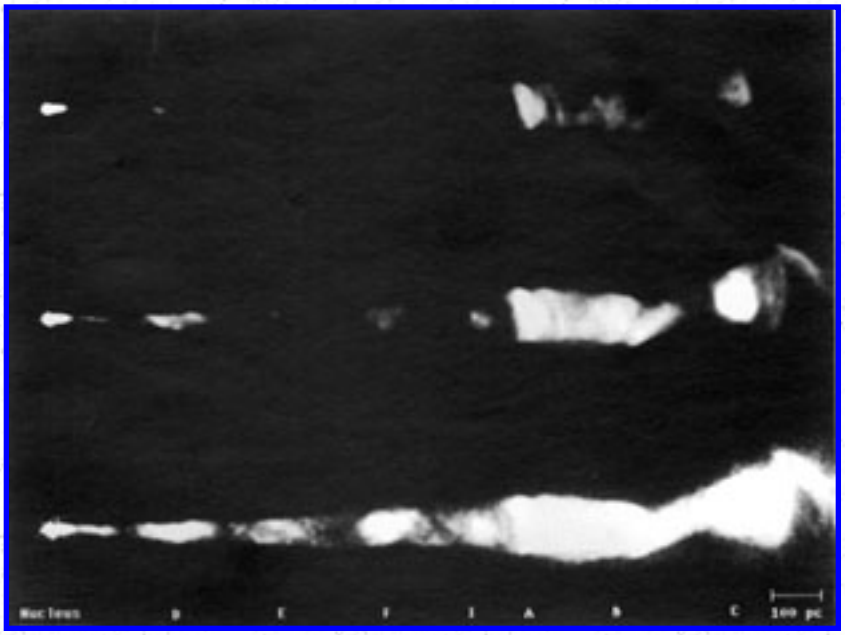

Figure 4. M87 jet at 15 GHz with 0.10" resolution. Approximately 40, 6, and 2 hrs. of VLA observation were used in the A, B, and C arrays, respectively. The intensity scale is linear, and white corresponds to 16, 5.5, and 1.8 mJy beam^{-1} in the top, middle, and bottom panels, respectively. The peak intensity at the nucleus is 2.34 Jy beam^{-1}. The knots are labeled at bottom, and the images are rotated so that up is towards P.A. 21°. Data from Biretta and Owen 1993.

I will refer to the region including knots A, B, and C as the "transition region" of the jet (Figure 5). Here the morphology suddenly changes from a cone with nearly straight walls, to a rough cylinder whose centerline wiggles back and forth, and whose diameter varies. While knot A is well aligned with the inner jet, knot B is displaced slightly south, and knot C slightly to the north. Also, the jet diameter appears to contract slightly between B and C, and then flare somewhat in knot C. This region also contains two remarkable "bright transverse features," which are bright linear regions that stretch across the jet, are oriented roughly normal to the jet axis, and are thin in the direction along the jet. The first is knot A, whose emission is dominated by a linear feature aligned 72 degrees to the jet's axis. The second is within knot C, whose emission is dominated by a feature roughly normal to the local jet axis. Knot B has a more complex, amorphous appearance.

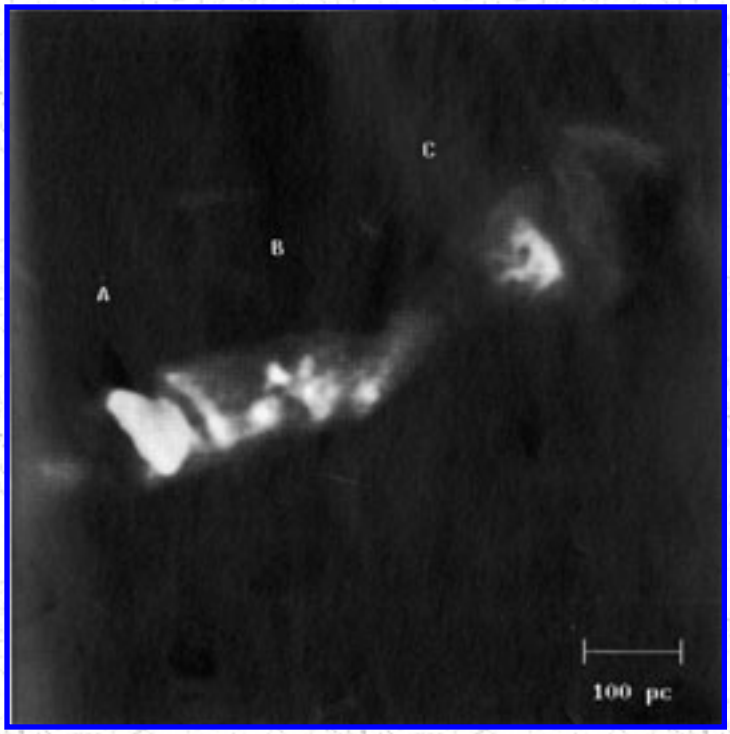

Figure 5. Detail of knot A, B, C region of the jet (i. e. "transition region") at 15 GHz with 0.10" resolution. The display intensities have been histogram equalized, and white corresponds roughly to 8 mJy beam^{-1}. North is up. From OHC89.

Another interesting feature of this region is a narrow dark lane which runs roughly along the centerline of the jet. It is most apparent in the region between knots A and B, and there is perhaps some evidence of it continuing into knot C.

The region beyond knot C is what I shall call the "outer jet." In this region the jet has strong side-to-side oscillations and bends sharply toward the south (Figure 6). After this bend the jet becomes indistinct and merges into the large amorphous lobe region west of the nucleus (Turland 1975). A similar lobe region is seen east of the nucleus, though there is no obvious jet here. Both lobes contain filamentary structures similar to those seen in the jet on mas and arcsecond scales (Hines, Owen, and Eilek 1989). We note that these lobes, while low in surface brightness, completely dominate the source flux at all radio frequencies. There also appears to be an exclusion between these radio lobes and the optical line emitting filaments; the optical line emission is mostly along and just beyond the northern and eastern boundaries of the radio lobe region (Ford and Butcher 1979; Jarvis 1990; Sparks, Ford, and Kinney 1993).

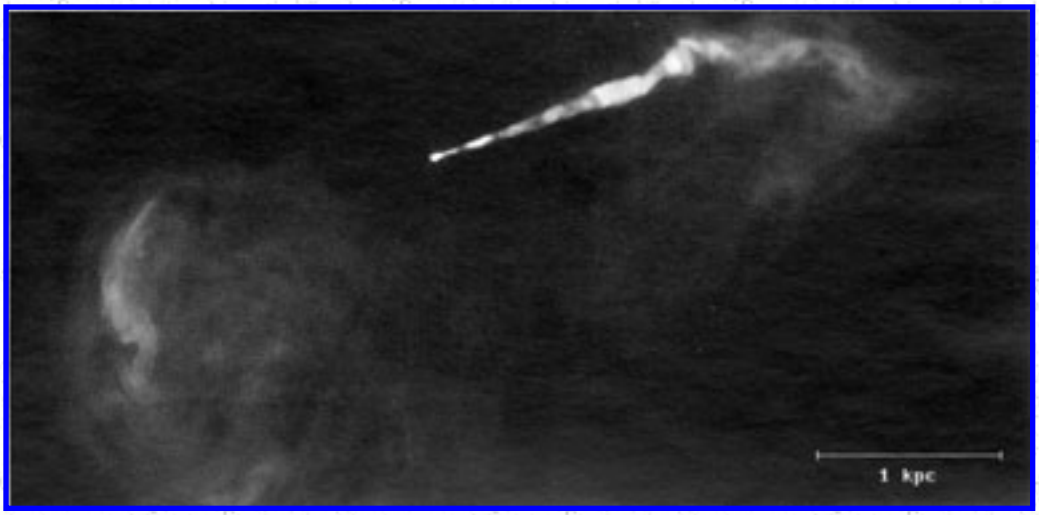

Figure 6. High dynamic range image of M87 jet and lobes at 15 GHz. The nucleus is near the center; total extent of the visible source is about 75" or 6 kpc. The resolution is 0.15", and the intensity scale is logarithmic with white corresponding to ~ 5 mJy beam^{-1}. Approximately 40, 6, and 2 hrs. of VLA observation were used in the A, B, and C arrays, respectively. North is up. From Biretta and Owen 1993.

At even larger scales "jet-like" structures again become evident (Figure 7). Here the lobes are only slightly resolved, and irregular, bent structures are seen extending to large distances from the lobe region. On the west side of the source, one of these extends for at least 35 kpc to the southwest, while on the east side another extends to about 19 kpc.

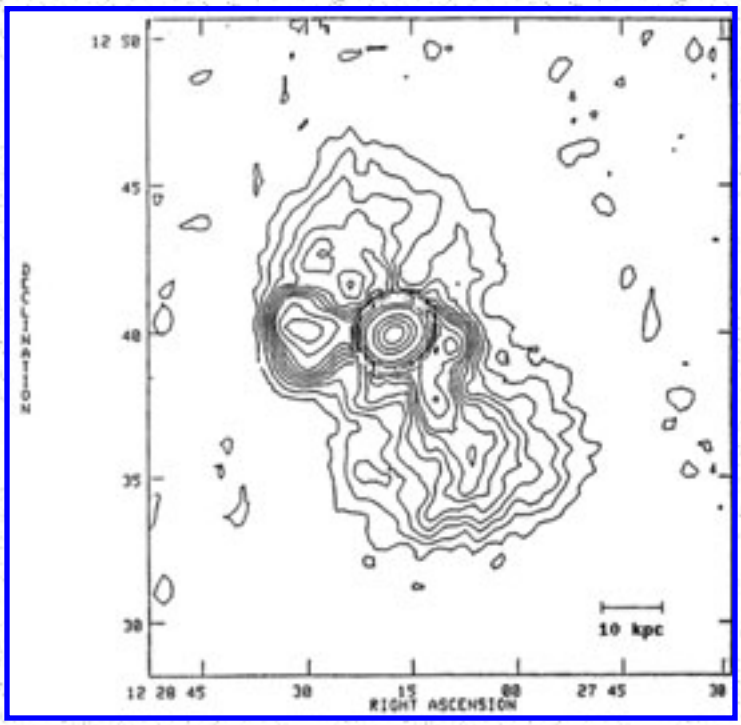

Figure 7. Low resolution image of M87 made with at 1.5 GHz with the VLA D configuration. The entire lobe region of Fig. 6 is contained in the bright, nearly unresolved region near the center. Jet-like structures or "plumes" are seen extending ~ 35 kpc towards the south-west and also towards the east. The resolution is ~ 100", and the brightest region has an intensity of 90 Jy beam^{-1}. North is up. From Owen (1992).

The magnetic field structure of the emission regions may be inferred from polarization images. While there are not yet any VLBI polarization images of the mas-scale jet, the polarization structure of the 20" jet has been studied in detail (OHC89; Fig. 8). The magnetic field runs roughly parallel to the jet everywhere, except in the bright transverse features (knots A and C) where it runs normal to the jet axis and along the transverse features. In general, wherever filamentary, linear, or elongated features are apparent, the field always runs along the length of the feature. Examples of such regions are seen in knots D and E, the brightest region of knot I, the region between knots B and C, the linear feature beyond knot C, and of course, the bright transverse features in knots A and C. This alignment between elongation and magnetic field is also seen in filamentary features of the lobes, the most notable being the bright north-south arc in the eastern lobe 25" from the nucleus (Owen 1992). Fractional polarizations are typically 15 to 30 percent throughout the jet, though some regions show polarizations as high as 50 to 70 percent. These latter values approach the maximum possible for synchrotron emission, and indicate highly ordered magnetic fields. There is also a tendency for fractional polarizations to be higher at the jet edges, especially in knots E, F, and I of the inner jet.

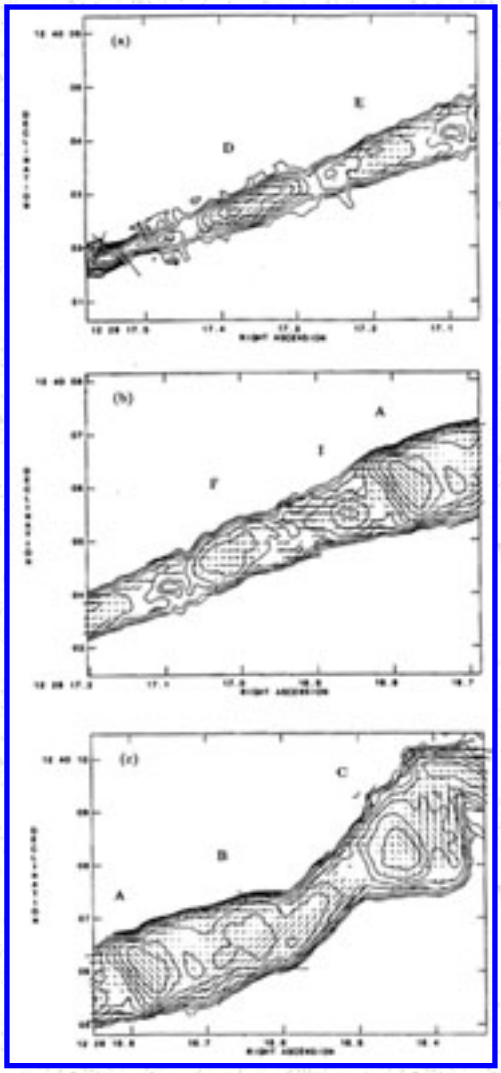

Figure 8. Contour plots of jet with vectors showing the local magnetic field direction at 15 GHz. The magnetic field lines are predominantly along the jet, except in knots A and C. A vector length of 1" corresponds to 216% polarization. Contours are space at factors of two in intensity beginning at 1.58 mJy beam^{-1}, and the resolution is ~ 0.15". (a.) Nuclear jet and knots D and E. Point source has been subtracted at nucleus. (b.) Knots E, F, I, and A. (c.) Knots A, B, and C. From OHC89.

Faraday rotation (the rotation of the polarization direction with increasing wavelength) can be used to measure the product of the electron density and the line-of-sight component of the magnetic field integrated along the line of sight. The Faraday rotation across the jet and lobes has been mapped at 5 GHz with 0.4 arcsecond resolution by Owen, Eilek, and Keel (1990). Rotations toward the jet are

typically between -300 and +300 radians m^2, while values in the lobes are much larger (+1000 to +2000 radians m^{-2}). This provides some evidence that the jet lies between the lobes and the observer. An otherwise inconspicuous "filament" of high-rotation lies in the east lobe and has typical rotations ~ +6000, with peak values ~ +8500 radians m^{-2}.

I conclude this section with a summary and some implications suggested by the observed morphology. We have seen that the "inner jet" between ~ 0.1 and ~ 1000 pc is quite straight, well collimated, and is often limb-brightened. The magnetic field is predominantly along the jet in this region, and the polarization is often highest at the jet edges. In the "transition region," which is delimited by two bright transverse features in knots A and C, the morphology begins to change. After each transverse feature the jet appears to become less stable, with stronger bends and kinks appearing on the side away from the nucleus. The opening angle of the visible jet is also reduced after each transverse feature; at knot A the diameter of the jet ceases to expand, and in the region beyond knot C the visible jet appears to become much narrower. The magnetic field direction also changes suddenly here, and runs almost normal to the jet in these features. In the "outer jet" region, including the jet beyond knot C, the lobes, and large-scale jet-like structures (1.6 to 40 kpc), the jet appears to have sharp bends and kinks, and is sometimes ill defined. We note that filamentary structures are ubiquitous in the source on all scales, and wherever polarization information is available the magnetic field is seen to run along these filaments.

It is tempting to interpret the straight, narrow inner jet as a high Mach number flow (*e.g.*, Bridle and Perley 1984, Sec. 6.1.4.), followed by shocks at the bright transverse features in knots A and C, and finally subsonic flow in the outer jet region (> 1.5 kpc). Shock waves have been long hypothesized in the M87 jet to provide particle acceleration and thus overcome the "lifetime" problem posed by the optical emission (*e.g.*, Graham 1970; Rees 1978; Blandford and Königl 1979a; *c.f.* Sec. 3.B.). The morphology of the bright transverse features, and their effect on the overall jet morphology, also suggests the presence of shocks. The bright transverse features might arise where shocks compress and amplify the magnetic fields, thus increasing the synchrotron emissivity (Biretta, Owen, and Hardee 1983). The perpendicular magnetic fields in these features would arise naturally, since only the component of the field in the plane of the shock front is amplified. (Presumably magnetic field of material flowing into the shock would contain some random component to be so amplified.) Furthermore, the increased bending and kinking of the jet after each transverse feature might result from reduction of the jet's Mach number after each shock, thus increasing its susceptibility to Kelvin-Helmholtz instability (Owen, Hardee, and Bignell 1980). The parallel magnetic fields seen for the inner jet might arise from shear in the jet's boundary layer, which would stretch randomly oriented field lines in the direction along the jet (*e.g.*, Begelman, Blandford, and Rees 1984, Sec. II.C.4.). We note that an alternative explanation for the transverse features has been proposed in which they are magnetic filaments wrapped around the surface of the jet (OHC89); however, the jet's reduced stability after knots A and C would still require (invisible) shocks or some additional explanation.

B. The Radio-to-X-Ray Spectrum of the Jet

In this section I will discuss spectra of the jet, as well as the optical and X-ray morphologies and their comparison to the radio. Figure 9 shows the spectra of the knots between various wavebands (Biretta, Stern, and Harris 1991, hereinafter BSH91). Care must be taken to use similar resolutions and integration regions at the different wavebands; here a resolution of ~ 1.2" is used and the brightness is integrated in contiguous boxes along the jet, with each box containing one knot. Unfortunately a different procedure must be used with the X-ray data, which involves PSF fitting and subtraction, but hopefully this is not a serious problem.

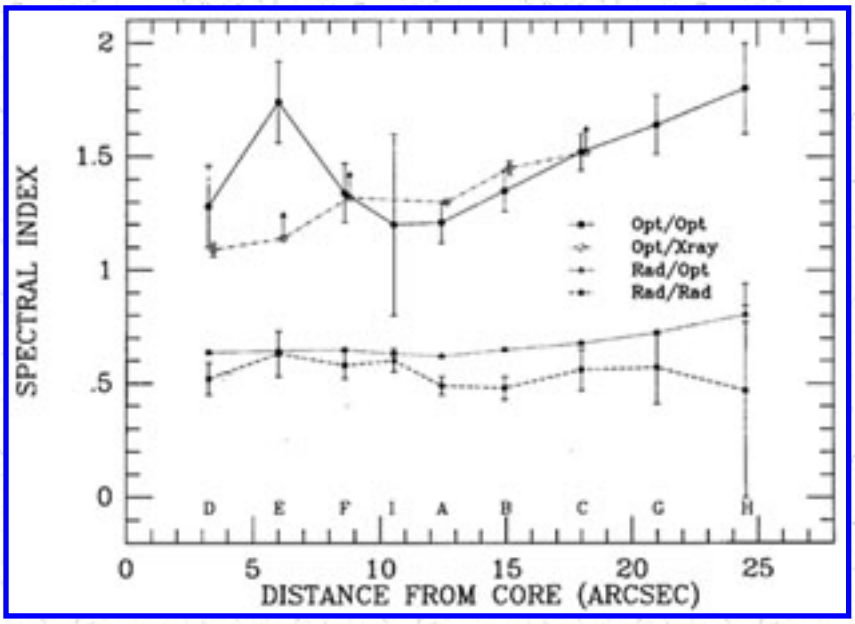

Figure 9. Spectral index of knots in M87 jet between various wavebands vs. distance from nucleus. Spectral index α defined as $S\nu \propto \nu^{-\alpha}$. Approximate positions of knots are labeled near bottom of plot. From BSH91.

All of the knots are roughly consistent with a radio spectral index α_{rr} of about 0.5 measured between 1.4 and 15 GHz, where the spectral index is defined in the sense $S\nu \propto \nu^{-\alpha}$. Large uncertainties near the end of the jet result from increasing difficulty in separating the "jet" from the background emission of the western "lobe" where the two begin to merge. There are no published results yet at higher resolution, but some preliminary work suggests the spectral index is probably slightly steeper (α ~ 0.6) between the knots than in the knot centers. Forster (1980) finds the spectral index of the western lobe (jetted lobe) is about 0.65, while the eastern lobe is steeper at about 0.85.

The radio-to-optical spectral indices are well determined, due largely to the huge frequency baseline between the radio and optical bands. For the inner jet (knots D, E, F, and I) and A the indices are all between α_{ro} = 0.62 and 0.65. After knot A there is a systematic steepening with increasing distance from the nucleus, so that between knots B and H α_{ro} steepens from 0.65 to 0.80. It is clear that the radio-to-optical spectrum is steeper than the radio spectrum, but whether this is caused by a gradual change above 15 GHz, or a sudden break near the optical band, is not known. Comparison of radio and ground-

based optical polarization images show that both the fractional polarizations, and polarization position angles, are very similar between these two bands (Schlötelburg, Meisenheimer, and Röser 1988; Fraix-Burnet, Le Borgne, and Nieto 1989). This strongly confirms that the optical emission is synchrotron emission and suggests much of it originates in the same physical volume as the radio emission.

The above indices are from ground-based optical images, and involve averaging over a large region encompassing each knot. It is possible to study the radio-to-optical spectral index, and the optical morphology, at ~ 0.1" resolution using the Hubble Space Telescope. Figure 10 compares two different deconvolutions of an HST Faint Object Camera image against a 15 GHz VLA image. This FOC image is a signal-to-noise optimized sum of 29 images made through various filters, with the overall intensity scaled to that at 372 nm wavelength. At first glance the HST and VLA images are remarkably similar (Boksenberg et al. 1992), though closer examination reveals a number of differences. The most pervasive difference is that the optical emission tends to be concentrated near the center of the jet and in the centers of the knots (Sparks, Biretta, and Macchetto 1993). This is most apparent for the inner jet (region encompassing knots D, E, F, and I). One manifestation is that the radio images show a low surface brightness component of emission which appears to fill the width of the jet, hence defining the jet edges, and also fills much of the regions between knots. This emission component appears to be very weak or absent at optical frequencies. Another manifestation is that the jet is narrower at optical frequencies than at radio frequencies. Figure 11 compares the intensity profiles across knot A and illustrates the narrower profile for the FOC data; similar differences are seen everywhere in the jet. Other differences in details of the structure are also apparent: The optical emission from knot E is mostly from a small region near the jet center, whereas the radio emission is from a more extended region. There are also striking differences in the structure between the nucleus and knot D, though this region is perhaps suspect at both wavebands due to deconvolution of the bright nucleus. Figure 12 shows the spectral index between the radio and FOC images, and illustrates many of the effects just noted. The flattest spectrum is seen in the brightest region of knot D with α_{ro} 0.5. In general the knot centers have indices ~ 0.6 and the inter-knot regions are steeper at ~ 0.7. We note that the 0.2" long jet in the nucleus (Fig. 3) has been detected in HST Planetary Camera images, and it appears to have a similar spectral index, α_{ro} ~ 0.74 (Lauer et al. 1992).

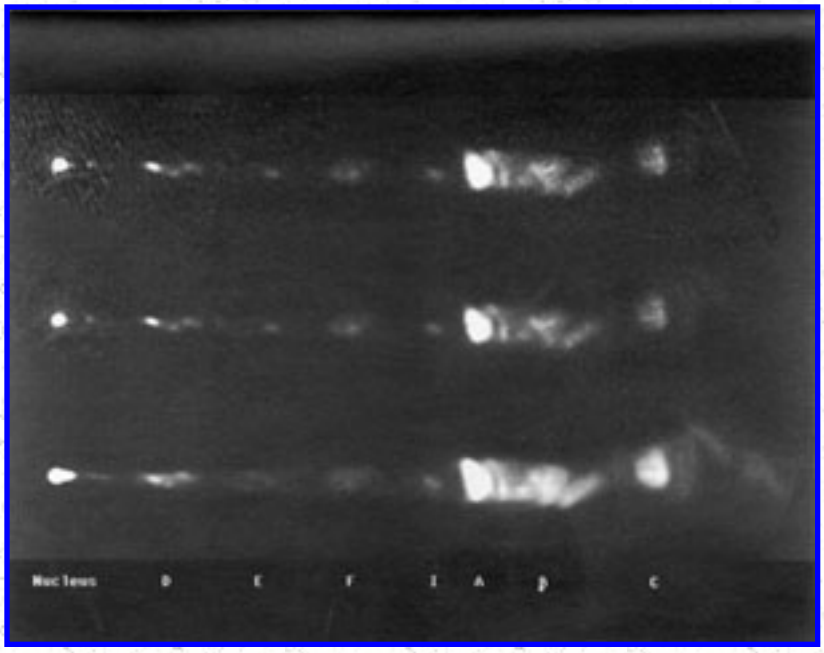

Figure 10. Comparison of optical and radio images of M87 jet at ~ 0.15" resolution. The optical images are composites of 29 HST FOC images scaled to an effective wavelength of 372 nm (806 THz). Both Fourier Quotient (top) and Lucy (middle) deconvolutions are shown. The radio image (bottom) is from 15 GHz VLA data. The images are rotated so that up is toward P.A. 21°. (a.) Low contrast image showing bright structures. Nucleus and knots are labeled along bottom of figure. (b.) High contrast image showing faint features. Original data from Sparks, Biretta, and Macchetto 1993. (Two small circular dark spots in radio image at knot F are photographic artifacts.)

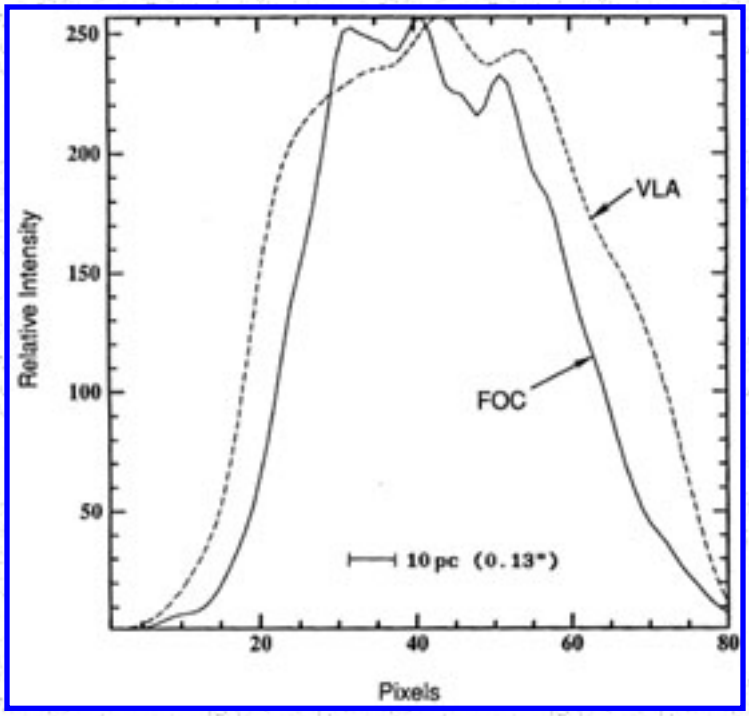

Figure 11. Comparison of radio (VLA 15 GHz) and optical (HST FOC 372 nm) intensity profiles across jet at the position of knot A. The jet appears appreciably narrower in the optical band. The intensities are arbitrarily scaled to give similar profile heights; resolution is ~ 0.10". The horizontal scale is in FOC pixels, with 1 pixel = 0.022".

Spectral indices within the optical band are more difficult to determine, and there is some controversy in this area. The short frequency baseline will exacerbate any small systematic errors, and differences in seeing and integration areas may also affect the results. For example, values of the optical spectral index of knot A, the brightest knot, range from α_{oo} ~ 0.57±0.05 (Keel 1988) to 1.21±0.09 (BSH91). Recently there appears to be some consensus developing for a value roughly between 0.9 and 1.0 (Perez-Fournon et al. 1988; Meisenheimer 1991; Zeilinger, Möller, and Stiavelli 1993). In any case, it appears fairly clear that the spectrum is appreciably steeper within the optical band than between the radio and optical. There is also agreement among different authors that knots of the inner jet have similar spectra, but that there is a systematic steepening after knot A which reaches $\delta\alpha$ ~ 0.5 around knot G. Meisenheimer (1991) reports evidence for steeper optical spectral indices between the knots by about $\delta\alpha$ ~ 0.1 as compared to the knot centers. Infrared and ultraviolet data (Stocke et al. 1981; Smith et al. 1983; Killeen et al. 1984; Perola and Tarenghi 1980; Sparks, Biretta, and Macchetto 1993) seem consistent with simple power-law interpolations between the radio, optical, and X-ray bands, provided corrections are made for differing aperture sizes (BSH91).

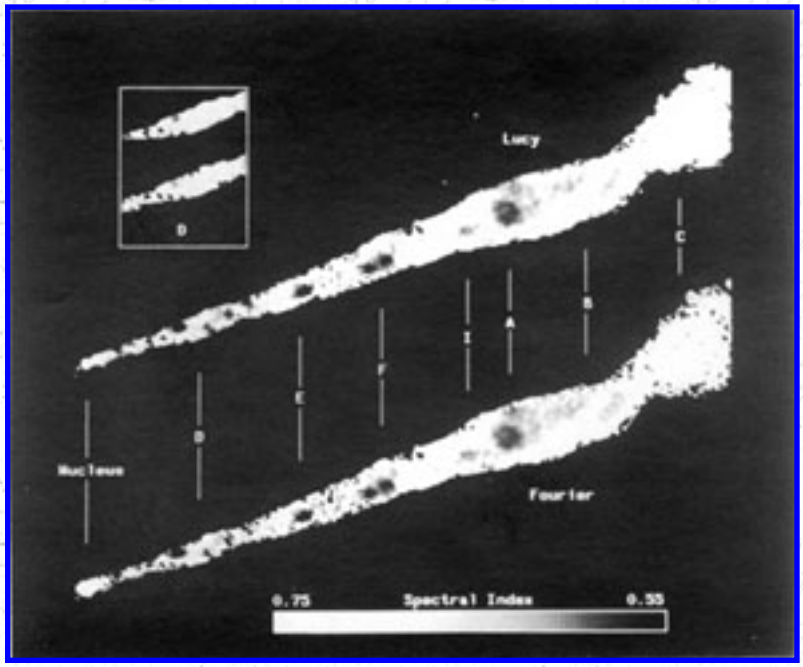

Figure 12. Radio to optical spectral index map at ~ 0.15" resolution using data from Fig. 10. The top image uses a Lucy deconvolution of the HST data, while the bottom image uses a Fourier Quotient deconvolution Spectral index runs from α = 0.75 (white) to α = 0.55 (black) and is defined as $S_\nu \propto \nu^{-\alpha}$. The inset shows knot D with a range from α = 0.65 to 0.45. North is up.

Einstein X-ray images with 3" resolution show two emission components (Schreier, Gorenstein, and Fiegelson 1982), and if the eastern one is aligned with the nucleus, we find that the western component aligns precisely with knot A (Figure 13). Subtracting these two dominant components reveals fainter emission at the positions of knots D and B (BSH91). Knot D has the flattest optical-to-X-ray spectral index of 1.08 ± 0.03. Knot A is steeper at α_{ox} = 1.30 ± 0.01, and B and C are steeper yet (Figure 9). The overall radio-to-X-ray spectrum is shown by Figure 14. The emission process for the X-rays is not entirely clear. Some support for synchrotron emission is provided by the consistency between the extrapolated optical spectrum and the observed X-ray flux, and by the trend for α_{ox} to steepen systematically between knots A, B, and C as seen for α_{ro} and α_{oo}, but these are circumstantial evidences at best.

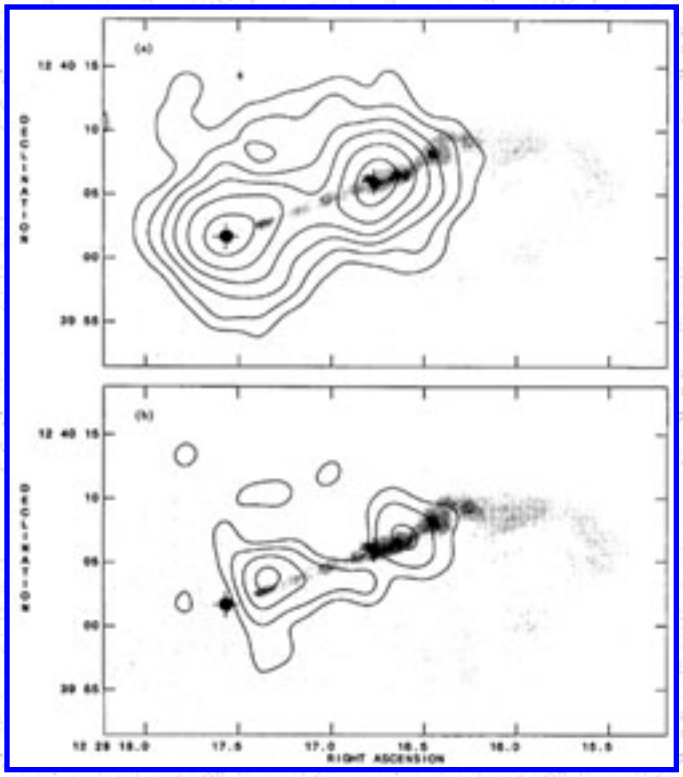

Figure 13. Comparison of radio (grey scale) and X-ray (contour plot) images of jet. The images have been aligned at the bright eastern component, which is assumed to be the nucleus in the X-ray image. (a.) X-ray image showing dominant emission components at nucleus and knot A. (b.) X-ray image with point sources subtracted at the positions of the nucleus and knot A (crosses). Weak emission is evident from knots D and B. From BSH91.

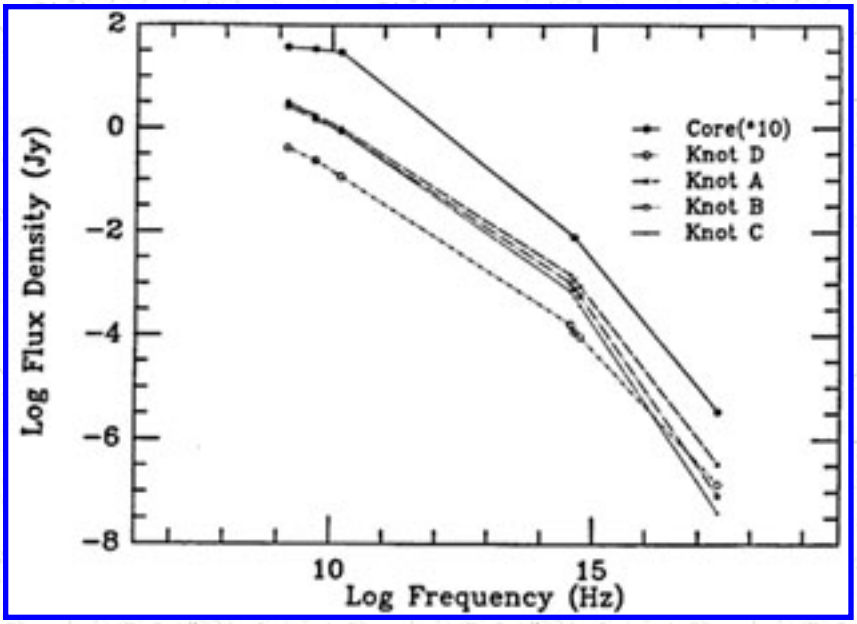

Figure 14. Radio to X-ray spectra of core and brightest knots in jet. While the spectra are generally similar, there is a trend for them to steepen with distance from the nucleus - knot D has the flattest spectrum, and knot C has the steepest. From BSH91.

We noted in Section B that there were systematic differences between the morphologies of the inner jet and the rest of the jet. Differences are also apparent in the spectra, and can be highlighted by constructing a Hertzsprung-Russell diagram for knots in the jet (Figure 15). Apparently knots of the inner jet all have similar α_{ro} and brightness, while the transition region and outer jet define a sequence of decreasing brightness and steepening spectra.

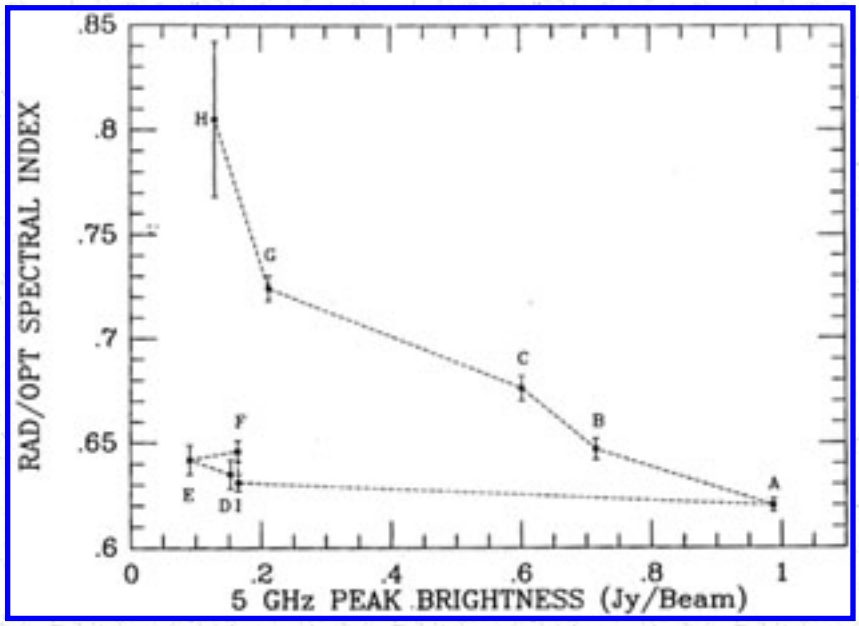

Figure 15. Hertsprung-Russell style diagram for knots in jet. The vertical axis shows radio (5 GHz) to optical (i band) spectral index, while the horizontal axis is radio peak brightness (Jy beam^{-1} at 5 GHz). The dashed line connects the knots in order of distance from the nucleus. Knots D, E, F, and I ("inner jet") occupy a small region, while knots A, B, C, G, and H define a sequence of steepening spectra and decreasing brightness. Knots of the inner jet (D, F, and I) have spectra similar to knot A, but are much fainter.

To summarize this section, we have seen that the optical and X-ray morphologies of the jet are remarkably similar to the radio. Throughout the jet the radio spectral index is ~ 0.5. The inner jet has α_{ro} ~ 0.65 and α_{oo} ~ 1.2, and the optical emission tends to concentrate in the knot centers. Knots A, B, and C ("transition" region) show steepening α_{ro}, α_{oo}, and α_{ox} with increasing distance from the nucleus, and

edges of the jet are optically weak. Beyond knot C ("outer jet") there is very little optical or X-ray emission.

C. Proper Motions in the Jet

It is possible to discern motions in the jet by comparing images made at several epochs. Comparisons of 1.7 GHz VLBI observations from three epochs have shown motion of feature N2 in the parsec-scale jet located about 20 mas (1.6 pc) from the core (Reid et al. 1989). This feature appears to move outward at an apparent speed of 0.28 ± 0.08 *c* (Figure 16).

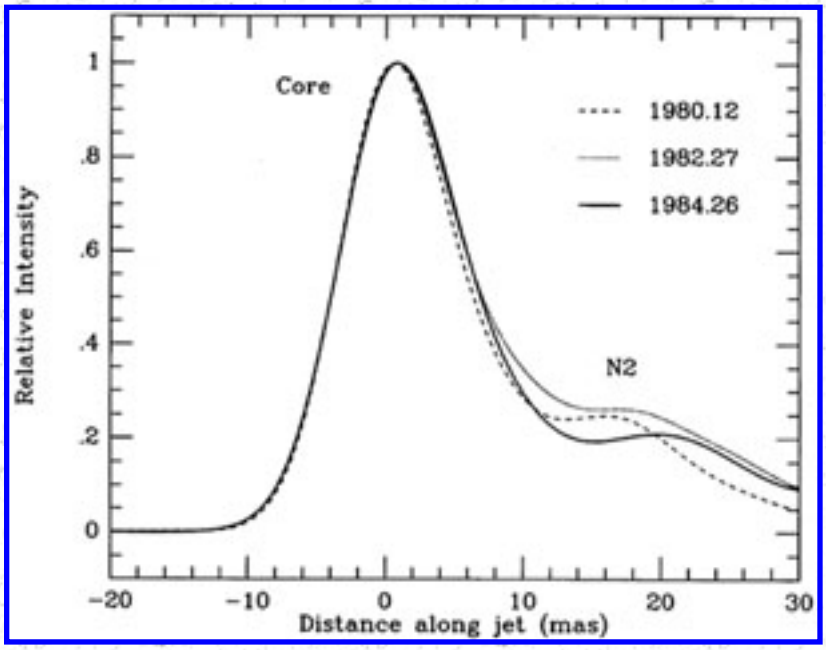

Figure 16. Intensity profiles through nucleus and along jet at 1.7 GHz with 8 mas resolution for epochs 1980, 1982, and 1984. The feature N2 appears to move away from the core at 1.1 ± 0.3 mas yr^{-1} (0.28 ± 0.08 c). From Reid et al. 1989.

Motions in the kiloparsec-scale jet have been detected by comparing high dynamic range 15 GHz VLA images observed at several epochs (Biretta and Owen 1990; Biretta and Owen 1993). The data are from two epochs in 1985, with another two in 1989. A fifth epoch from 1982 has poor dynamic range, but provides useful information on knot A. After an initial "cross-calibration" (Mason 1986) against the 26 Feb. 1985 data, each epoch was reduced independently and in the same manner. Final images were made using the Maximum Entropy Method and data from the A, B, and C configurations of the VLA. Small changes in the positions of features were then measured using a two-dimensional cross-correlation technique (Biretta, Owen, and Cornwell 1989, hereinafter BOC89). Because of the high sensitivity of the cross-correlation technique, and the high dynamic range of the images, it is possible to measure position changes to an accuracy better than 1 percent of the 0.15 arcsecond resolution of the images.

The results for knot A, the brightest knot, are shown in Figure 17a. Here *changes* in the position of knot A relative to the 26 Feb. 1985 reference position are plotted against epoch. This knot appears to move away from the nucleus with a proper motion of 2.06 ± 0.11 mas yr^{-1}, which corresponds to an apparent speed of 0.52*c* ± 0.03*c*, where *c* is the velocity of light. The two-dimensional cross-correlation technique also measures any position change in the transverse direction. Any such motion normal to the jet axis is very small in knot A, with the formal value being -0.025*c* ± 0.035*c* (Figure 17b). Together the two components of motion give a net motion directly away from the nucleus.

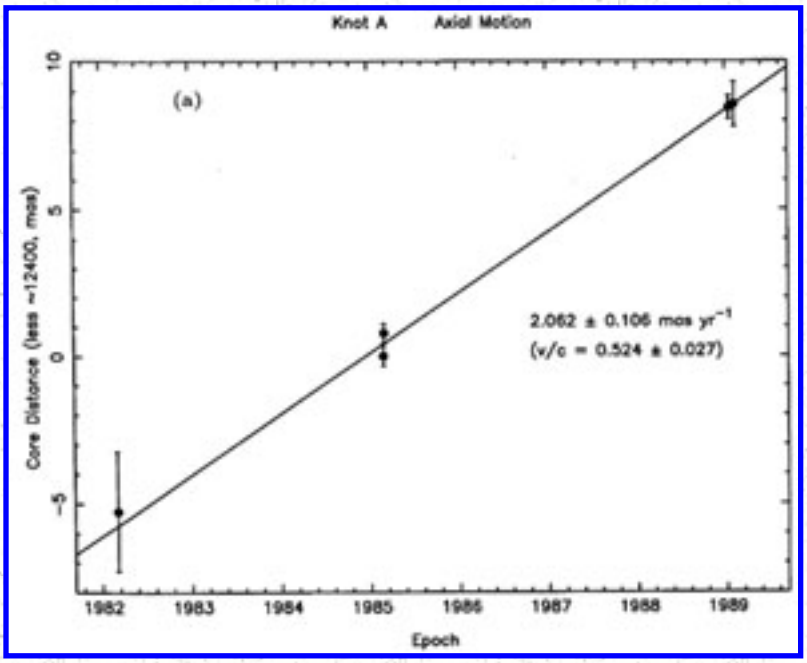

Figure 17. Motion of knot A relative to the nucleus. (a.) Axial component of motion (along jet axis). Knot A moves away from the nucleus at 2.06 ± 0.11 mas yr^{-1} or 0.52c ± 0.03c.

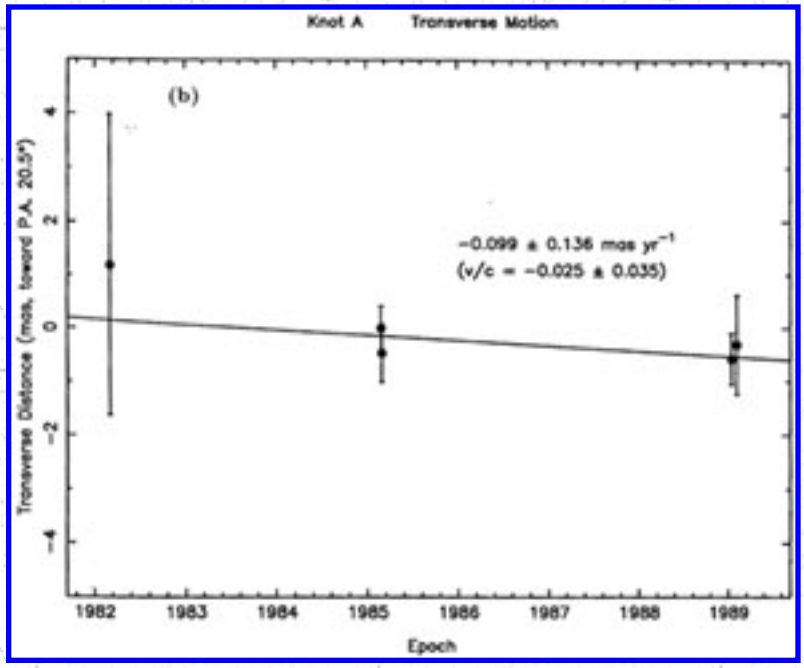

Figure 17. (Continued.) (b.) Transverse component of motion (normal to jet axis). There is essentially no motion in direction normal to the jet axis. In both plots zero distance is arbitrarily set to the epoch 1985.1 position. Results are derived from 15 GHz VLA images with 0.15" resolution. From Biretta and Owen 1993.

The same technique can be applied to other bright knots, and the results are shown in Figure 18 as vectors plotted on the respective knots. Knots D and B, located about 200 and 1200 pc from the nucleus, show outward motion at $0.66c \pm 0.15c$ and $0.63c \pm 0.09c$, respectively. Knot C, located near the end of the jet, is appreciably slower at $0.12c \pm 0.07c$. Neither knots D nor A, which are located in the region where the jet is quite straight, show significant motion normal to the jet axis. However, both knots B and C, which are located in the region where the jet begins to bend and kink, show significant transverse motion at $-0.24c \pm 0.05c$ and $0.23c \pm 0.09c$, respectively (positive transverse motion means towards P.A. 70 degrees).

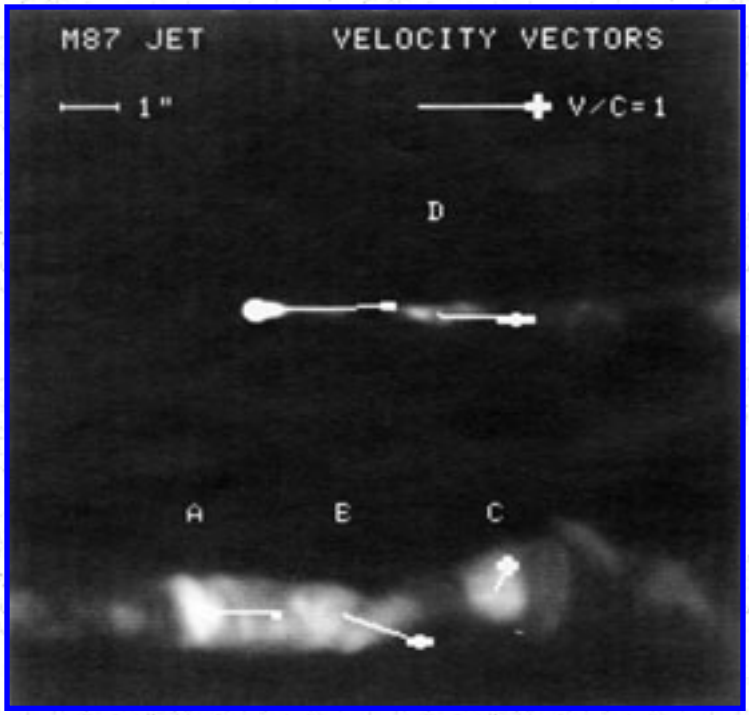

Figure 18. Observed velocity vectors superimposed on radio image of the jet. The velocities are derived from 5 epochs of 15 GHz VLA observations between 1982 and 1989. The velocity scale is indicated by the vector at the upper right; the heavy cross at the head of each vector illustrates its uncertainty. The jet is split into two pieces for photographic reasons; the nucleus and inner jet are in the top panel; knots A, B, and C are in the bottom panel. Data from Biretta and Owen 1993.

This technique can also measure motions for smaller condensations within the knots, and this has produced interesting results. For three condensations within knot D we obtain speeds $0.13c \pm 0.17c$, $1.7 \pm 0.4c$, and $3.0 \pm 0.4c$, the latter two with velocity vectors pointing straight down the jet. Five different condensations in knot B give speeds ranging from $-0.4c \pm 0.3c$ to $1.3 \pm 0.2c$. Significant transverse motions are seen for some of these condensations in knot B - which, again, are located where the jet begins to bend and kink. These results suggest that some of the knots have a significant degree of internal turbulence, or at least cannot be thought of as simple rigid structures sliding down the jet.

There is some element of uncertainty in these proper motion results, primarily because the technique is new, and there is as yet no independent confirmation. We note that similar work in 3C120 has produced conflicting results (Walker, Walker, and Benson 1988; Muxlow and Wilkinson 1991). Observations with the Space Telescope offer the possibility of a completely independent confirmation of these results.

D. Evidence for the Presence of a Counter-Jet

The twin-relativistic jet model of Blandford and Rees (1974) supposes that the central engine is rotationally symmetric and should produce two diametrically opposed jets. The fact that M87 has two lobes and two jet-like structures on large scales (> 1.5 kpc) supports such a picture, but efforts to detect a counter-jet on scales $\lesssim$ 1 kpc have been entirely unsuccessful. Limits on the ratio of the jet to counter-jet brightness have been derived from radio data, and a conservative limit is > 150:1 (BOC89). A somewhat stronger limit (> 380:1) can be obtained if we assume the counter-jet would appear identical to the jet, but this is perhaps a poor assumption, since light travel time effects (among others) could cause the jet and counter-jet to look very different. The limiting factor here is not the quality of the radio images, but rather the radio emission from the lobes, whose complex morphology could easily camouflage a weak counter-jet. Stronger limits of > 450:1 are obtained in the optical (Stiavelli, Möller, Zeilinger 1992), where the galaxy light presents a simple background which is easily subtracted.

An important advance in this area is the recent discovery of an optical "hot spot" which is placed precisely where we might expect the end of the counter-jet to be located (Stiavelli et al. 1992; Sparks, Macchetto, and Owen 1992; Figure 19). This hot spot can also be seen in older images in the literature (*e.g.*, Keel 1988). This new feature is located opposite the jet to a precision well within the jet's width. And its distance from the nucleus of 25" places it at a distance corresponding to knot H at the end of the visible jet. It is spatially coincident with a bright arc of emission seen in the radio. It is virtually certain that the emission from this feature is synchrotron emission, and not, for example, line emission. It is seen in at least three optical bands (V, R, and I), and both its radio-to-optical spectral index (0.86) and optical spectral index (1.9 ± 1.0) are similar to those of knot H. Furthermore, its optical polarization properties are similar to those of the spatially coincident radio emission. (We note this new feature appears unassociated with Arp's counter-jet (1967) which is slightly more distant from the nucleus, and consists primarily of line emission.)

Figure 19. Comparison of optical and radio morphology of hot spot in M87 east radio lobe (inside boxes on left). The optical image (top) is the sum of I, R, and V band observations; the radio image (bottom) is from 15 GHz VLA observations. Nucleus is near center of each panel with the jet extending towards the right. North is up.

This optical hot spot provides evidence for an unseen counter-jet, because the lifetime of the electrons emitting at these frequencies is very short. At radio frequencies the electron lifetime is about 10^6 years, so that the radio emission can be ascribed to events in the distant past. However, the lifetime for the optically emitting electrons in the hot spot is only about 1.6×10^3 years, indicating that something is supplying high-energy electrons at nearly the present epoch. The most obvious candidate for such a supply is some sort of unseen counter-jet.

3. MODELS AND PROBLEMS

In this section I review models for the observations, as well as several problems and their possible solutions. I begin with the problem of confining the jet. Next I consider models for the radio-to-X-ray spectrum and problems posed by the short lifetimes of the optical (and X-ray) emitting electrons. Finally a possible model for the jet kinematics is sketched out.

A. Confinement of the Jet

If we assume the jet is a steady-state structure, then some external pressure must act to counter the jet's internal pressure, in order to confine the jet and maintain its narrow appearance. That is, a static pressure balance must exist between the jet and external medium. It is possible to estimate both the pressure in the emitting regions and the external pressure, and test for such a balance. The minimum pressure required to provide the observed synchrotron luminosity may be estimated from the usual synchrotron calculations (*e.g.*, Moffet 1975). The resulting pressure is proportional to the observables as

$$P_{min} \propto (AL/V)^{4/7},$$

where L is the luminosity, V is the source volume, and A is a weak function of the spectral shape. The largest uncertainty in this calculation is perhaps the source volume. For example, if we assume the emissivity is uniform across the jet's radius we obtain a pressure $P_{min} = 5 \times 10^{-9}$ dyne cm^{-2} for knot A (Owen, Hardee, and Bignell 1980), while a larger pressure $P_{min} = 2 \times 10^{-8}$ dyne cm^{-2} results if we assume the emission originates in a thin layer near the jet's surface (OHC89; Fig. 20). The external pressure maybe estimated from cooling accretion flow models fit to X-ray observations of the thermal

emission (*e.g.*, Lea, Mushotzky, and Holt 1982; Schreier, Gorenstein, and Feigelson 1982; White and Sarazin 1988). At the distance from the nucleus of knot A, typical estimates of the external pressure are $P_{ext} \sim 6 \times 10^{-10}$ dyne cm^{-2}. This is much less than either estimate of the minimum pressure in knot A, and suggests a problem in confining the jet and explaining its narrow appearance. A similar situation exists for most other knots in the jet.

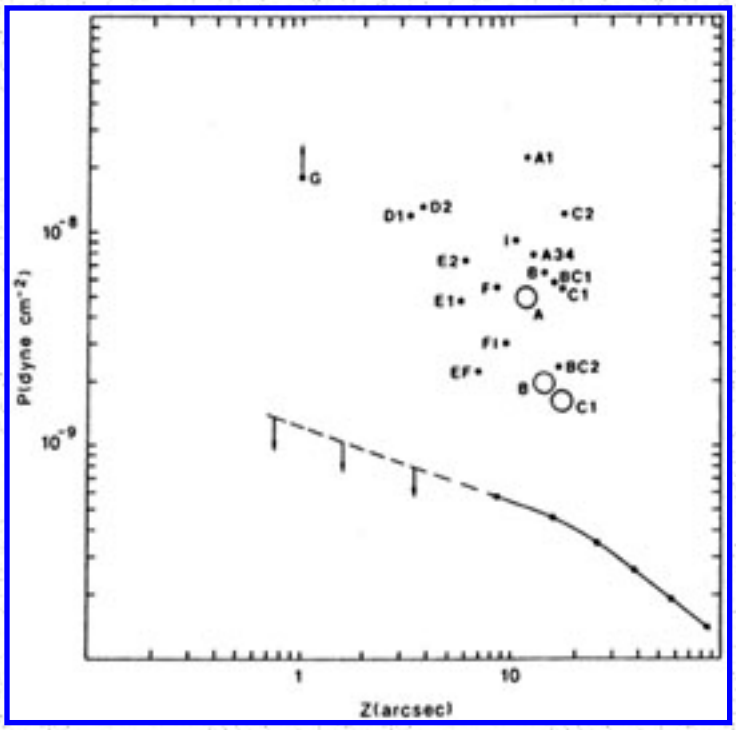

Figure 20. Comparison of minimum internal pressures in the knots with external pressures derived from models of X-ray observations. Dots show internal pressures derived by OHC89, while large circles show values derived from largest source volume consistent with the radio observations. Line shows estimated external pressure. Original Figure from OHC89.

One solution is that our initial assumption of static pressure balance is incorrect. As we have discussed in Section 2.A., it seems likely that knots A and C are shock waves, and hence the emitting material may be in a region of transient expansion, rather than static pressure balance. Another solution is that the jet is freely expanding and confined only by its own inertia, in which case there is again no pressure balance. This possibility seems most applicable to the inner jet (region including knots D, E, F, and I), which appears to be an expanding cone, and may represent a high Mach number flow (*c.f.* Sec. 2.A.). These two solutions together would appear to resolve the confinement problem everywhere in the jet except knot B (Biretta, Owen, and Hardee 1983). Knot B appears as a non-expanding cylinder, and contains no obvious shock-like structures. Here it may be necessary to invoke magnetic confinement, where magnetic field lines wrapped around the jet serve to amplify the external pressure, and thereby

confine the jet (Benford 1978). This is not necessarily inconsistent with the polarization observations (OHC89) showing the magnetic field to be oriented along the jet in knot B, since the confining field could lie mostly outside the visible jet.

In summary, confinement of the jet appears to be a serious problem only in the region of knot B, and perhaps magnetic effects play a role here.

B. Models for the Radio-to-X-Ray Spectrum and the Particle Lifetime Problem

It is virtually certain that the radio and optical emission are both produced by the synchrotron process. This is due to the high degree of polarization, and the similar polarization properties at these two bands (*c.f.* Sec. 2.B.). The cause of the X-ray emission is much less clear, and we now discuss several possibilities.

In principle, the X-ray emission could be thermal emission from small regions surrounding the knots. If we assume the largest emission region consistent with the knots appearing unresolved in the Einstein HRI images (~ 2"), and a temperature of 1 KeV, the observed X-ray luminosity of knot A requires a pressure of 1.4×10^{-8} dyne cm^{-2}. This is much larger than the external pressure (Sec. 3.A.) so a thermal X-ray emitting region cannot be confined. Inverse Compton X-ray emission is also a possibility, but it is difficult to get enough X-ray luminosity from the observed radio-to-optical synchrotron spectrum; a large excess of infrared photons or low energy electrons ($\gamma < 100$) must be invoked (BSH91).

X-ray synchrotron emission seems like the best possibility, though it is not completely without problems. The strongest evidence for X-ray synchrotron emission, is that the X-ray flux lies close to the extrapolated optical-ultraviolet spectrum for several of the knots (Fig. 14; BSH91; Sparks, Biretta, and Macchetto 1993). There is no evidence for it comprising a separate spectral component. Furthermore, the radio-to-X-ray spectra of the different knots have similar shapes, suggesting the X-rays are somehow related to the shorter wavelengths. The problems arise when attempting to model the shapes of the radio-to-X-ray spectra. All the knots show a spectral break near, or just below, optical frequencies. If we simply compare α_{ro} to α_{ox} we find the breaks range from $\delta\alpha \sim 0.5$ for knot D, to $\delta\alpha \sim 0.8$ for knots A, B, and C. These latter values are larger than produced by continuous particle injection models with synchrotron losses ($\delta\alpha = 0.5$, Kardashev 1962). And models with a sudden cessation of particle injection produce high frequency spectra which are too steep - $\alpha \sim 1.67$ (Pacholczyk 1970) or an exponential cutoff (Jaffe and Perola 1974).

A problem related to the high frequency spectra, is the short lifetime of the electrons producing the optical (and X-ray) synchrotron emission. The lifetime of these electron is short, and yet optical and X-ray emission is seen at large distances from the nucleus. The lifetime for a synchrotron emitting electron to lose its energy is proportional to

$$\tau \propto \nu^{-1/2} B^{-3/2},$$

where ν is the observation frequency, and *B* is the magnetic field strength. Assuming equipartition fields, the lifetime of the radio emitting electrons is $\gtrsim 10^5$ years, and the nucleus can supply radio emitting electrons to the entire source. However, at optical frequencies the lifetime is only ~ 100 years (and only ~ 10 years for the X-rays if they are synchrotron emission), and yet optical and X-ray emission is seen more than 3000 l.y. from the nucleus. Furthermore, the optical spectra of knots D, E, F, I, and A are all rather similar (Figure 9); there is no evidence for a systematic steeping with distance from the nucleus until after knot A. Several solutions have been proposed, though none seems without problems. First-order Fermi acceleration at shocks could re-accelerate the electrons (*e.g.*, Rees 1978), however few of the knot look like shocks. For example, knots D, E, F, I, and A have similar spectra, but only A looks like a shock. A modification of this idea might be to have particle acceleration everywhere (from turbulent to shock regions), but acceleration models tend to give spectra which are strongly dependent on the compression ratio (Ellison, Jones, and Reynolds 1990). A different solution is to propose the energetic electrons are transported along the jet without radiative losses. In one version, OHC89 propose a low magnetic field "pipe" at the jet center which supplies the knots. A similar idea, is that the energetic electrons are propagated in a relativistic flow ($\gamma \sim 10$) where time dilation prevents losses (Begelman 1992; *c.f.* Felten 1968, Meisenheimer 1991).

C. A Model for the Jet Kinematics

In this section I derive various constraints on the jet kinematics, and build a possible model for the jet. Some ingredients of the model have already been discussed in Section 2.A., where morphological considerations lead to a picture where the inner jet represents a high Mach number supersonic flow (knots D, E, F, and I), the jet's Mach number is reduced (slowed) at shocks in the transition region (knots A, B, and C), and finally the outer jet (knots G, H, lobes, *etc.*) is a region of unstable subsonic flow.

In section 2.C. we presented evidence for apparent motions in the jet, and these can be used to constrain both the speed and direction of motion for these features. Since it is possible that the visible "patterns" in the jet and the jet "fluid" move with different speeds (*e.g.*, Lind and Blandford 1985), we consider the pattern and fluid speeds, $\beta_{\rm pattern}$ and $\beta_{\rm fluid}$, separately. The usual relationship for superluminal motion (Blandford and Königl 1979b),

$$\beta_{obs} = \frac{\beta_{pattern} \sin\theta}{1 - \beta_{pattern} \cos\theta},$$

can be used to derive constraints on the pattern speed $\beta_{\rm pattern}$ and angle between the direction of motion and the line of sight θ from the observed speed $\beta_{\rm obs}$, where all speeds are in units of the velocity of light.

For example, the observed speeds of knot A, and the fastest features in knots B and D, yield lower limits on $\beta_{pattern}$ of 0.48*c*, 0.78*c*, and 0.95*c*, and lower limits on the Lorentz factor $\gamma_{pattern}$ of 1.1, 1.6, and 3.2, respectively. The observed speeds here for knots A and B are not large enough to constrain θ, but the speed for the fast region of knot D requires $\theta_D < 37° \pm 5°$, where the uncertainty results from the formal uncertainty on the observed proper motion. Since this feature in knot D is seen to move directly away from the nucleus, it seems reasonable to assume its motion is along the jet axis, and hence the jet axis is positioned within about 37° of the line of sight ($\theta_{\text{jet axis}} \sim 37°$).

An additional constraint can be garnered from the sharp feature or "edge" seen in knot A. Presumably this edge is a two-dimensional structure seen apparently edge-on. To see this sharp edge, the photons traveling toward the observer must remain within the plane of the structure as both they, and the two-dimensional structure itself, move. This constraint requires $\beta_{pattern} \sim \cos\theta$ (Biretta, Owen, and Hardee 1983; Eichler and Smith 1983); otherwise, relativistic aberration will cause the plane containing the two-dimensional structure to appear less "edge-on," or even "face-on." A more generalized geometry might allow the plane containing the edge to be at some angle $90° + \epsilon$ to the jet axis (Reid et al. 1989; BOC89) and the resulting constraint is

$$\cot\theta_{jet\,axis} = \frac{\tan\epsilon + \beta_{pattern}\sec\epsilon}{\sqrt{1-\beta^2_{pattern}}}.$$

The observed angle between the edge and the jet axis measured on the plane of the sky is ~ 72°, suggesting $|\epsilon|$ could be at least 18°; we will adopt $|\epsilon| \leq 30°$ as a limiting value. This constraint from the aberration of knot A is plotted in Figure 21, along with constraints from the observed proper motion of knot A's edge and the fast feature in knot D. The two constraints for knot A's edge result in $\theta \gtrsim 35°$ and $\beta_{pattern} \sim 0.4$ for knot A. Assuming the jet axis is straight between knots D and A, and combining their constraints, we estimate that the jet axis is about 40° from the line-of-sight ($\theta_{\text{jet axis}} \sim 40°$).

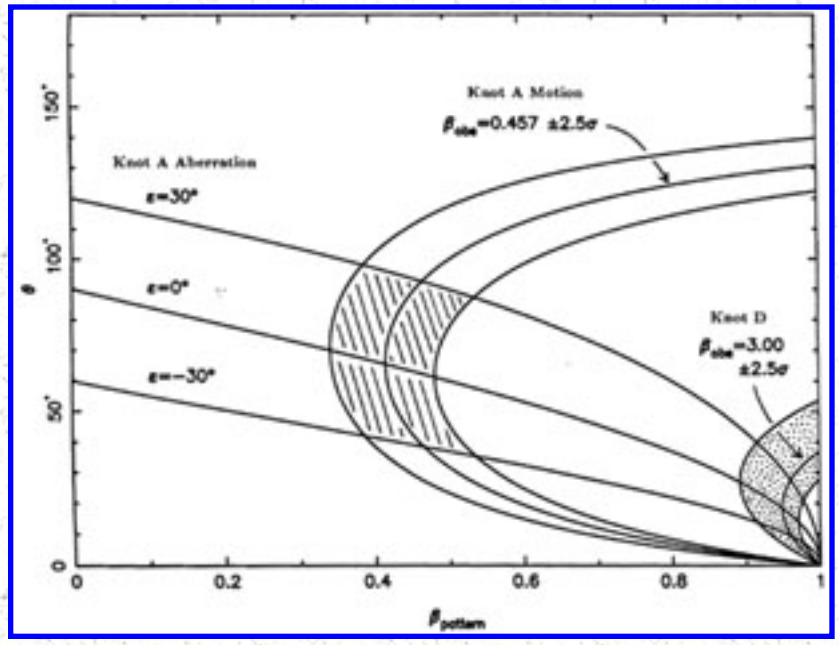

Figure 21. Constraints on the angle between the jet axis and line-of-sight (θ) and pattern speed of jet features ($\beta_{pattern}$) derived from (a) observed motion of knot A edge at β_{obs} = 0.457c, (b) appearance of sharp edge in knot A together with relativistic aberration ($|\varepsilon| < 30°$), and (c) observed motion of fast feature in knot D at β_{obs} = 3.0c. The knot A constraints together require $\theta > 35°$, while that from knot D requires $\theta < 54°$. Taken together these yield $\theta \sim 40°$.

So far we have considered only the *pattern* speeds of features in the jet. The more interesting parameter is the speed of the jet *fluid* itself. Here the arguments are unfortunately less direct. Non-relativistic numerical simulations of jets (*e.g.*, Norman, Winkler, and Smarr 1984) have found that the fluid speed tended to be at least twice that of the visible patterns. From the derived pattern speeds $\beta_{pattern} \gtrsim 0.5$ in much of the jet, this would appear to imply at least $\beta_{fluid} \gtrsim 0.5$, and perhaps $\beta_{fluid} \sim 1$ if relativistic effects can be ignored. Other indirect evidence can be taken from statistical studies of superluminal quasars, where Cohen (1990) finds similar mean values for the Lorentz factors of the fluid and pattern.

We also note that "scissor effects," which are sometimes cited as a possible cause of $\beta_{pattern} > \beta_{fluid}$ (*e.g.*, Hardee and Norman 1989; Fraix-Burnet 1990), must be relatively unimportant in the M87. A scissor effect might be created, for example, at the intersection of a pair of shock waves. While the individual waves might move slowly, their intersection point could, in principle, attain any speed. However, we note the moving features in knots D and A show motion directly down the jet. And while outward motion is seen in at least eight regions, no regions show significant *inward* motion. It would seem contrived if the observed motions, and especially those in knots D and A, were produced by the intersection of shock waves, rather than some mechanism closely tied to the jet flow.

A constraint on the fluid speed may also be derived from the ratio of jet to counter-jet brightness and the usual formulae for relativistic beaming (Blandford and Königl 1979b). As we have seen (Sec. 2.D.) there is considerable evidence for the presence of a counter-jet of some sort. If we assume it has an intrinsic brightness equal to that of the visible radio jet, and use the limit on the brightness ratio $R > 150$ derived from 15 GHz VLA observations (BOC89) we have

$$\mathrm{R} = \left(\frac{1 + \beta_{fluid} \cos \theta_{jet\ axis}}{1 - \beta_{fluid} \cos \theta_{jet\ axis}} \right)^{2.5} > 150$$

which may be solved for the limits $\beta_{\mathrm{fluid}} > 0.76$ ($\gamma_{\mathrm{fluid}} > 1.5$) and $\theta_{\mathrm{jet\ axis}} < 40°$. We note that the stronger ratio $R > 450$ from optical measurements (Stiavelli, Möller, and Zeilinger 1992) produces slightly weaker limits on the derived parameters, because of the steeper optical spectral index. If a shock in knot A does reduce the fluid speed, as we have suggested, it maybe necessary to treat the "inner jet" and "transition region" separately, and this gives slightly weaker limits for each region than given above. The main uncertainty with these calculations, of course, is the assumption that the unseen counter-jet has an intrinsic brightness similar to the visible jet. It is possible they have intrinsic differences, or that there are *apparent* differences caused by rapid evolution and time delay between the jet and more distant counter-jet.

Finally, we have a brief look at the kinematics of knot A under the assumption that it is a strong shock. If we presume that the fluid speed of the inner jet is not too different from the derived pattern speed of the fast region in knot D, then we have $\gamma_{\mathrm{fluid}} \gtrsim 3$ for the inner jet. Knot A must therefore be treated as a relativistic shock, for which material has a downstream velocity of $c/3$ relative to the shock (Blandford and Rees 1974). When added to the observed motion of knot A, and assuming $\theta_{\mathrm{jet\ axis}} \sim 40°$, we obtain an apparent speed of $0.9c$ for the material in the downstream region. This is at least roughly consistent with speeds in 4 out of 5 regions of knot B, which range from $O.6c \pm 0.2c$ to $1.3c \circ 0.2c$.

Therefore, to summarize our proposed model of the kinematics (Fig. 22): The inner jet (nucleus to knot A) is a high Mach number flow with a Lorentz factor $\gtrsim 3$ and oriented about 40° from the line-of-sight. There is a shock at knot A, about 1 kpc from the nucleus, where the flow speed is reduced to $\gamma_{\mathrm{fluid}} \sim 1.4$ relative to the nucleus. A second shock in knot C further reduces the jet speed such that beaming becomes relatively unimportant, and at larger distances the jet is a subsonic, buoyant plume. It seems virtually certain that a counter-jet is present, though of course, details of its structure are unknown. This model is built upon, and explains, the following evidence: (1) overall jet morphology, consisting of straight inner jet (< 1.0 kpc), gradual bending in transition region, and sharp bends in outer jet (> 1.6 kpc); (2) presence of transverse features in knots A and C; (3) magnetic field normal to jet axis in knots A and C; (4) superluminal speeds up to $3c$ for knot D; (5) motion and appearance of sharp edge in knot A; (6) lower observed speeds in most of knot B ($0.6c$ to $1.3c$); and (7) symmetric source structure (*i.e.* two-sided structure) on scales $\gtrsim 2.0$ kpc. It is interesting to reflect that many elements of this model are

suggested in early papers (*e.g.*, Rees 1978).

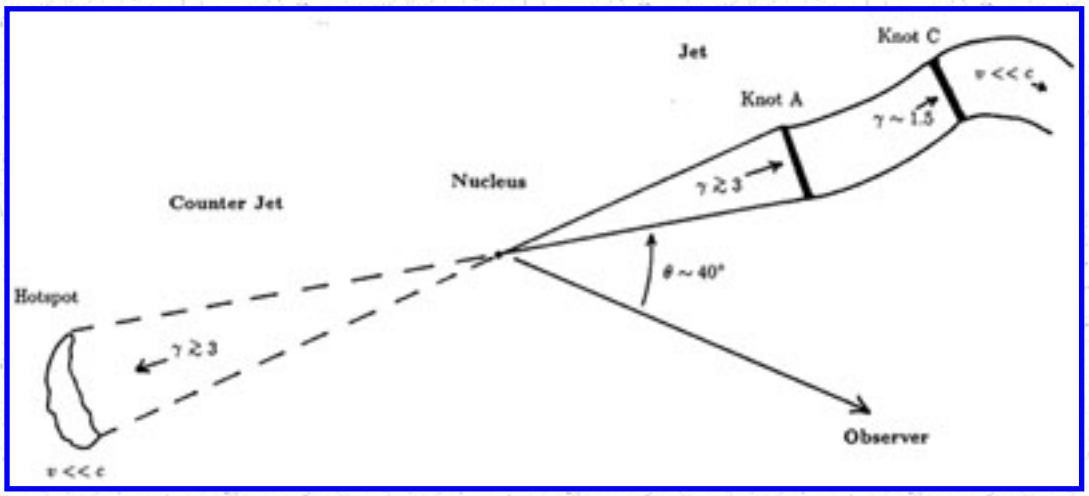

Figure 22. Suggested model for M87 jet and counter-jet. Initially the jet is relativistic with $\gamma \gtrsim 3$, but then slows in knots A and C to v << c ($\gamma \sim 1$). The jet axis is oriented about 40° from the line of sight. The counter-jet is invisible over much of its length due to relativistic beaming, and perhaps intrinsic faintness as well. At the hotspot it is slowed and becomes visible.

A model of this type may have several additional benefits. As mentioned in Section 3.B., time dilation effects associated with relativistic flow along the inner jet might allow energetic electrons to travel farther from the nucleus, thereby reducing the particle lifetime problem posed by the optical emission. The knot spectra are similar until knot A, at which point they steepen systematically with increasing distance - which could be attributed to a sudden reduction in the jet velocity knot A. In terms of other FR-I radio sources, a relativistic "inner jet" might account for the one-sided jet "bases" seen in many of these sources (Bridle 1986). These one-sided bases are typically straight, well collimated, and 2 to 20 kpc in length (*e.g.*, Bridle 1984; Eilek et al. 1984; Leahy, Jagers, and Pooley 1986; O'Dea and Owen 1986), and thus resemble the inner jet of M87. Only on larger scales does the structure become two-sided and poorly collimated, and suggests non-relativistic flow (*e.g.*, Scheuer 1987). Furthermore, a relativistic inner jet would be consistent with $\gamma \gtrsim 5$ on the parsec scale, as required by unified models which propose that FR-I radio sources are the parent population of BL Lac objects (Urry, Padovani, Stickel 1991, and references therein). We note that $\gamma_{fluid} \gtrsim 5$ is not ruled out by our observations, and that such regions would appear very dim due to beaming and $\theta_{jet\ axis} \sim 40°$.

One concern about the model proposed here is the slow velocity seen in the nucleus by VLBI techniques. Component N2 appears to move outward at only ~ 0.3*c* (Reid et al. 1989). This could be attributed to $\beta_{pattern} << \beta_{fluid}$, but this makes M87 rather different from quasar nuclei where $\beta_{pattern} \sim \beta_{fluid}$ seems common, although cases of "slow" features are not unknown (Shaffer and Marscher 1987). Also, the large angle we propose between the jet axis and line of sight would make any features with

$\gamma_{pattern} \approx \gamma_{fluid} \gtrsim 5$ appear very dim. Future VLBI monitoring may clarify this situation, if as components are seen in the M87 nucleus. Another concern regards the disposition of the inner jet's bulk kinetic energy after knot A. If the jet is suddenly decelerated at knot A, where is this energy going? It does not seem to go into radiation, since the luminosity of knot A is not that much greater than the other knot's; and the jet remains collimated, so it probably does not go into internal pressure. However, it is unclear how much kinetic energy is being carried by the inner jet; it is possible that the jet is very light (*i. e.* low mass density) and therefore carries relatively little bulk kinetic energy. A related concern is the high luminosity of the lobes, which is presumably supplied by the jet. However, this luminosity is dominated by low frequency radio emission, and these electrons have extremely long lives. It may be adequate to merely supply energetic electrons, rather than bulk kinetic energy, to the lobes. If we ignore adiabatic expansion, and assume luminous plasma flowing through knot B at $\beta \sim 0.7$ merely inflates the lobes, then the lobe luminosity could be supplied in 10^5 years (which is less than electron lifetimes at low radio frequencies).

4. SUMMARY AND FUTURE WORK

We have reviewed the current observational status of the M87 jet, as well as several models and problems suggested by the data. To briefly summarize:

1. High resolution observations show the jet is well collimated on scales from about 1 to 1000 pc, with evidence collimation extending down to scales ~ 0.01 pc. Beyond 1 kpc the jet passes through "shock-like" structures, becomes unstable and poorly collimated, but yet continues to scales ~ 35 kpc.

2. The optical and X-ray morphology of the 25" (2 kpc) jet, except for a few systematic trends, is nearly identical to the radio morphology. Knots along the inner jet have similar radio-to-optical spectra, thus creating the "particle lifetime" problem.

3. Comparison of radio images from different epochs give evidence for proper motions with typical apparent speeds between 0.5*c* and 1.0*c*. Speeds up to 3*c* are seen for the inner jet.

4. The recent discovery of an optical continuum hot spot opposite the jet strongly suggests a counter-jet is present.

5. The emission regions within the jet appear to be out of pressure balance with the surrounding interstellar medium. It is possible that some of these regions are freely expanding, while others may be shocks. The most serious confinement problems appear in knot B, and magnetic effects may be able to provide confinement.

6. It is difficult to produce the observed radio-to-X-ray spectrum with existing models.

7. We have outlined a kinematic model wherein the first kpc of the jet moves with a relativistic velocity ($\gamma \gtrsim 3$). The jet is then slowed at several shocks, and finally proceeds outward to distances ~ 35 kpc at sub-relativistic speeds. In this model the inner jet is aligned about 40° from the line of sight.

Future VLA observations, as well as monitoring with HST, are needed to confirm the observed motions. As speeds are measured for more regions, it may be possible to assemble and observed flow diagram, and hence perform detailed tests of numerical models. VLBI monitoring may clarify the situation at pc-scales, where low velocities have been seen. Combined radio, infrared, optical, UV, and X-ray observations at similar resolution ($\lesssim$ 1") are needed to assemble a detailed spectrum of the jet, both in the knots and inter-knot regions. This may elucidate the cause of the optical spectral break and the process responsible for the X-rays. Theoretical and numerical models are needed which address the possibility of relativistic flow for the inner jet, and the consequences this may have for M87 and other FR-I sources.

REFERENCES

1. Arp, H. C. 1967, ApLett, 1, 1
2. Baade, W. and Minkowski, R. 1954, ApJ, 119, 215
3. Baath, L. B. et al. 1992, A&A, 257, 31
4. Begelman, M. C., Blandford, R. D., and Rees, M. J. 1984, Rev. Mod. Phys., 56, 255
5. Begelman, M. C. 1992, private communication.
6. Benford, G. 1978, MNRAS, 183, 29
7. Biretta, J. A., Owen, F. N., and Hardee, P. E. 1983, ApJL, 274, L27
8. Biretta, J. A., Owen, F. N., and Cornwell, T. J. 1989, ApJ, 342, 128 (BOC89)
9. Biretta, J. A., Owen, F. N., 1990, in Parsec-scale Jets, eds. J. A. Zensus and T. J. Pearson, (Cambridge: Cambridge Univ. Press), 125
10. Biretta, J. A., Stern, C. P., and Harris, D. E. 1991, AJ, 101, 1632 (BSH91)
11. Biretta, J. A. and Owen, F. N., 1993, in preparation.
12. Blandford, R. D. and Rees, M. J. 1974, MNRAS, 169, 395
13. Blandford, R. D. and Königl, A. 1979a, ApLett, 20, 15
14. Blandford, R. D. and Königl, A. 1979b, ApJ, 232, 34
15. Boksenberg, A., Macchetto, F. et al. 1992, A&A, 261, 393
16. Bolton, J. G., Stanley, G. J., and Slee, O. B. 1949, Nature, 164, 101
17. Bridle, A. H. and Perley, R. A. 1984, ARA&A, 22, 319
18. Bridle, A. H. 1984, AJ, 89, 979
19. Bridle, A. H. 1986, Can. J. Phys., 64, 353
20. Cohen, M. H., 1990, in Parsec-scale Jets, eds. J. A. Zensus and T. J. Pearson, (Cambridge: Cambridge Univ. Press), 317
21. Curtis, H. D. 1918, Pub. Lick Obs., 13, 31

22. de Vaucouleurs, G. and Nieto, J.-L. 1979, ApJ, 231, 364
23. Eichler, D. and Smith, M. 1983, Nature, 303, 779
24. Eilek, J. A., Burns, J. O., O'Dea, C. P., and Owen, F. N. 1984, ApJ, 278, 37
25. Ellison, D. C., Jones, F. C., and Reynolds, S. P. 1990, ApJ, 360, 702
26. Fanaroff, B. L. and Riley, J. M. 1974, MNRAS, 167, 31p
27. Felten, J. E. 1968, ApJ, 151, 861
28. Ford, H. C. and Butcher, H. 1979, ApJS, 41, 147
29. Forster, J. R. 1980, ApJ, 238, 54
30. Fraix-Burnet, D., Le Borgne, J.-F., and Nieto, J.-L., 1989, A&A, 224, 17
31. Fraix-Burnet, D., 1990, A&A, 227, 1
32. Fraix-Burnet, D, et al. 1990, AJ, 101, 88
33. Graham, I. 1970, MNRAS, 149, 319
34. Hardee, P. E. and Norman, M. L. 1989, ApJ, 342, 680
35. Hines, D. C., Owen, F. N., and Eilek, J. A. 1989, ApJ, 347, 713
36. Jaffe, W. J. and Perola, G. C. 1974, A&A, 26, 423
37. Jarvis, B. J. 1990, A&A, 240, L8
38. Kardashev, N. S. 1962, SvA, 6, 317
39. Keel, W. C. 1988, ApJ, 329, 532
40. Killeen, N. E. B., Bicknell, G. V., Hyland, A. R., and Jones, T. J. 1984, ApJ, 280, 126
41. Lauer, T. R., et al. 1992, AJ, 103, 703
42. Lea, S. M., Mushotzky, R. F., and Holt, S. S. 1982, ApJ, 261, 42
43. Leahy, J. P., Jagers, W. J., and Pooley, G. G. 1986, A&A, 156, 234
44. Lind, K. R. and Blandford, R. D. 1985, ApJ, 295, 358
45. Liu, F. K. and Xie, G. Z. 1992, A&ASS, 95, 249
46. Masson, C. R. 1986, ApJ, 302, L27
47. Meisenheimer, K. 1991, in Physics of Active Galactic Nuclei, eds. W. Duschl and S. Wagner, (Berlin: Springer-Verlag), 525
48. Moffet, A. T. 1975, in Galaxies and the Universe: Stars and Stellar Systems vol. 9, eds. A. Sandage, M. Sandage, and J. Kristian (Chicago: Chicago Univ. Press), 211
49. Muxlow, T. W. B. and Wilkinson, P. N. 1991, MNRAS, 251, 54
50. Norman, M. L., Winkler, K.-H. A., and Smarr, L. 1984, in Physics of Energy Transport in Extragalactic Radio Sources, eds. A. H. Bridle and J. A. Eilek, (Green Bank: NRAO), 150
51. O'Dea, C. P., and Owen, F. N. 1986, ApJ, 301, 841
52. Owen, F. N., Hardee, P. E., and Bignell, R. C. 1980, ApJ, 239, L11
53. Owen, F. N., Hardee, P. E., and Cornwell, T. J. 1989, ApJ, 340, 698 (OHC89)
54. Owen, F. N., Eilek, J. A., and Keel, W. C. 1990, ApJ, 362, 449
55. Owen, F. N. 1992, private communication
56. Pacholczyk, A. G. 1970, Radio Astrophysics, (San Francisco: Freeman)
57. Perola, G. C. and Tarenghi, M. 1980, ApJ, 240, 447

58. Perez-Fournon, I., Colina, L., Gonzalez-Serrano, J. I., and Biermann, P. L. 1988, ApJL, 329, L81
59. Rees, M. J. 1978, MNRAS, 184, 61p
60. Reid, M. J., Biretta, J. A., Junor, W., Spencer, R., Muxlow, T. 1989, ApJ, 336, 125
61. Schlötelburg, M., Meisenheimer, K., and Röser, H.-J. 1988, A&A, 202, L23
62. Schreier, E. J., Gorenstein, P., and Feigelson, E. D. 1982, ApJ, 261, 42
63. Shaffer, D. B. and Marscher, A. P. 1987, in Superluminal Radio Sources, eds. J. A. Zensus and T. J. Pearson, (Cambridge: Cambridge Univ. Press), 67
64. Smith, R. M., Bicknell, G. V., Hyland, A. R., and Jones, T. J. 1983, ApJ, 266, 69
65. Sparks, W. B., Fraix-Burnet, D., Macchetto, F., and Owen, F. N. 1992, Nature, 355, 804
66. Sparks, W. B., Ford, H. C., and Kinney, A. L. 1993, ApJ, in press
67. Sparks, W. B., Biretta, J. A., and Macchetto, F. 1993, in preparation
68. Spencer, R. E. and Junor, W. 1986, Nature, 321, 753
69. Stiavelli, M., Möller, P., and Zeilinger, W. W. 1992, Nature, 354, 132
70. Stiavelli, M., Biretta, J., Möller, P., and Zeilinger, W. W. 1992, Nature, 355, 802
71. Stocke, J. T., Rieke, G. H., and Lebofsky, M. J. 1981, Nature, 294, 319
72. Tonry, J. L. 1991, ApJ, 373, L1
73. Turland, B. D. 1975, MNRAS, 170, 281
74. Urry, C. M., Padovani, P., and Stickel, M. 1991, ApJ, 382, 501
75. Walker, R. C., Walker, M. A., and Benson, J. M. 1988, ApJ, 335, 668
76. White, R. E., III and Sarazin, C. L. 1988, ApJ, 335, 688
77. Zeilinger, W. W., Möller, P., and Stiavelli, M. 1993, MNRAS, in press